as DOE (design of experiments) are powerful tools for synthesis (*30*–*32*), yet they typically focus on performing minimal numbers of experiments, as large numbers of experiments are often resource- and time-intensive to conduct. However, because large numbers of experiments are readily feasible with this nanomole-scale chemistry platform, we were able to construct a three-factorial, four-level response surface modeling experiment to study the loading of catalyst against varying stoichiometries of base and nucleophile in the reaction of chloride **6** with amine **10**. In this DOE experiment, each condition was repeated twice, resulting in 128 total reactions with <3 mg of **6**. Indeed, a high-quality response surface model was generated with the nanomole-scale chemistry approach (Fig. 2D), which helped to define the critical charges of nucleophile and base for optimal reaction performance. The optimized conditions used 15 mol % **42** at 0.05 M concentration; by translating to more practical conditions of 5 mol % **42** and 0.24 M concentration, we obtained full conversion and a 79% isolated yield of **46** on a 25-mg scale, which was reproduced to obtain a 76% isolated yield on a 1-g scale (Fig. 2D). This result shows that advanced statistical reaction analysis, which is typically reserved for chemistry opportunities where material is plentiful, can be applied to reactions in the material-limited front lines of drug discovery or natural product synthesis.

In biomedical research, chemical synthesis should not limit access to any molecule that is designed to answer a biological question. This work demonstrates an example of how conditions for complex Pd-catalyzed C-O, C-N, and C-C cross-coupling reactions can be evolved into a powerful, substrate-focused approach to chemistry miniaturization to overcome limited access to complex products. With innovative research, other high-value modern chemistry reactions could be similarly designed into this paradigm to improve synthesis in material-limited environments by evolution of catalysts and reagents to perform in DMSO, NMP, or other high-boiling solvents at ambient temperature.

REFERENCES AND NOTES

1. M. R. Friedfeld *et al.*, *Science* **342**, 1076–1080 (2013).
2. D. A. DiRocco *et al.*, *Angew. Chem. Int. Ed.* **53**, 4802–4806 (2014).
3. D. W. Robbins, J. F. Hartwig, *Science* **333**, 1423–1427 (2011).
4. A. McNally, C. K. Prier, D. W. C. MacMillan, *Science* **334**, 1114–1117 (2011).
5. K. D. Collins, T. Gensch, F. Glorius, *Nat. Chem.* **6**, 859–871 (2014).
6. R. Moreira, M. Havranek, D. Sames, *J. Am. Chem. Soc.* **123**, 3927–3921 (2001).
7. S. M. Preshlock *et al.*, *J. Am. Chem. Soc.* **135**, 7572–7582 (2013).
8. A. Bellomo *et al.*, *Angew. Chem. Int. Ed.* **51**, 6912–6915 (2012).
9. J. R. Schmink, A. Bellomo, S. Berritt, *Aldrichim. Acta* **46**, 71–80 (2013).
10. M. Peplow, *Nature* **512**, 20–22 (2014).
11. T. Rodrigues, P. Schneider, G. Schneider, *Angew. Chem. Int. Ed.* **53**, 5750–5758 (2014).
12. S. Monfette, J. M. Blacquiere, D. E. Fogg, *Organometallics* **30**, 36–42 (2011).
13. P. M. Murray, S. N. G. Tyler, J. D. Moseley, *Org. Process Res. Dev.* **17**, 40–46 (2013).
14. S. D. Roughley, A. M. Jordan, *J. Med. Chem.* **54**, 3451–3479 (2011).
15. T. W. J. Cooper, I. B. Campbell, S. J. F. Macdonald, *Angew. Chem. Int. Ed.* **49**, 8082–8091 (2010).
16. A. Nadin, C. Hattotuwagama, I. Churcher, *Angew. Chem. Int. Ed.* **51**, 1114–1122 (2012).
17. Merck internal study of electronic notebooks.
18. M. M. Hann, G. M. Keserü, *Nat. Rev. Drug Discov.* **11**, 355–365 (2012).
19. F. Lovering, J. Bikker, C. Humblet, *J. Med. Chem.* **52**, 6752–6756 (2009).
20. H. A. Malik *et al.*, *Chem. Sci.* **5**, 2352–2361 (2014).
21. R. E. Tundel, K. W. Anderson, S. L. Buchwald, *J. Org. Chem.* **71**, 430–433 (2006).
22. D. S. Surry, S. L. Buchwald, *Chem. Sci.* **2**, 27–50 (2011).
23. N. C. Bruno, M. T. Tudge, S. L. Buchwald, *Chem. Sci.* **4**, 916–920 (2013).
24. T. Ishikawa, Y. Kondo, H. Kotsuki, T. Kumamoto, D. Margetic, K. Nagasawa, W. Nakanishi, in *Superbases for Organic Synthesis: Guanidines, Amidines, Phosphazenes and Related Organocatalysts*, T. Ishikawa, Ed. (Wiley, West Sussex, UK, ed. 1, 2009), pp. 1–326.
25. Compounds were generally purified by MS-directed purification. Isolated yields ranged from 1 to 100%, but we made no attempt to maximize the isolated yields in these reactions and instead focused on obtaining high-purity compounds as quickly as possible, which is typical in most medicinal chemistry campaigns. Some reactions showed product formation by UPLC-MS analysis but were either insufficiently pure or too low in yield for purification.
26. M. Liu *et al.*, *ACS Comb. Sci.* **14**, 51–59 (2012).
27. Some electrophiles were not fully soluble in DMSO, so NMP was used instead. Even though three stock solutions in NMP still displayed mild insolubility, the TTP Mosquito operates on positive-displacement pipetting, so viscous solutions or suspensions of small particulates are easily transferred.
28. W. Schafer, X. Bu, X. Gong, L. A. Joyce, C. J. Welch, in *Comprehensive Organic Synthesis*, C. J. Welch, Ed. (Elsevier, Oxford, ed. 2, 2014), vol. 9, pp. 28–53.
29. C. J. Welch *et al.*, *Tetrahedron Asymmetry* **21**, 1674–1681 (2010).
30. J. C. Ianni, V. Annamalai, P.-W. Phuan, M. Panda, M. C. Kozlowski, *Angew. Chem. Int. Ed.* **45**, 5502–5505 (2006).
31. S. E. Denmark, C. R. Butler, *J. Am. Chem. Soc.* **130**, 3690–3704 (2008).
32. K. C. Harper, M. S. Sigman, *Science* **333**, 1875–1878 (2011).

ACKNOWLEDGMENTS

We thank S. Krska, M. Tudge, G. Hughes, and E. Parmee for helpful discussions; M. Liu, E. Streckfuss, T. Meng, N. Pissarniski, and W. Li for assistance in purification of compounds; M. Christensen and J. Voigt for experimental assistance; and S. M. O'Brien and M. McColgan for graphic design. S.B. was supported by an NSF GOALI Grant associated with the University of Pennsylvania. Supported by the MRL Postdoctoral Research Fellows Program (A.B.S. and E.L.R.).

SUPPLEMENTARY MATERIALS

www.sciencemag.org/content/347/6217/49/suppl/DC1
Materials and Methods
Supplementary Text
Figs. S1 to S32
Tables S1 to S11
References (*33*–*40*)
Data Files S1 to S5

25 July 2014; accepted 11 November 2014
Published online 20 November 2014;
10.1126/science.1259203

REPORTS

QUANTUM OPTICS

Quantum harmonic oscillator state synthesis by reservoir engineering

D. Kienzler,* H.-Y. Lo, B. Keitch, L. de Clercq, F. Leupold, F. Lindenfelser, M. Marinelli, V. Negnevitsky, J. P. Home*

The robust generation of quantum states in the presence of decoherence is a primary challenge for explorations of quantum mechanics at larger scales. Using the mechanical motion of a single trapped ion, we utilize reservoir engineering to generate squeezed, coherent, and displaced-squeezed states as steady states in the presence of noise. We verify the created state by generating two-state correlated spin-motion Rabi oscillations, resulting in high-contrast measurements. For both cooling and measurement, we use spin-oscillator couplings that provide transitions between oscillator states in an engineered Fock state basis. Our approach should facilitate studies of entanglement, quantum computation, and open-system quantum simulations in a wide range of physical systems.

Reservoir engineering is a method in which specially designed couplings between a system of interest and a zero-temperature environment can be used to generate quantum superposition states of the system as the steady state of the dissipative process, independent of the initial state of the system (*1*–*3*). Theoretical work has shown the potential for using such engineered dissipation for universal quantum computation (*4*) and in providing new routes to many-body states (*5*–*7*). Experimentally, these techniques have been used to generate entangled superposition states of qubits in atomic ensembles (*8*), trapped ions (*9*, *10*), and superconducting circuits (*11*). Theoretical proposals for quantum harmonic oscillator state synthesis by reservoir engineering extend from trapped ions (*2*, *3*) to superconducting cavities (*12*, *13*) and nanomechanics (*14*).

Here, we experimentally demonstrate the generation and stabilization of quantum harmonic oscillator states by reservoir engineering based on the original proposal of Cirac *et al.* (*1*), which we use to generate and stabilize squeezed,

Institute for Quantum Electronics, ETH Zürich, Otto-Stern-Weg 1, 8093 Zürich, Switzerland.
***Corresponding author. E-mail: daniel.kienzler@phys.ethz.ch (D.K.); jhome@phys.ethz.ch (J.P.H.)**

displaced-squeezed, and coherent states. Making use of engineered spin-motion couplings that are closely related to those used in the reservoir engineering, we introduce measurement techniques that provide simple spin population dynamics, allowing us to directly verify the coherence of the states produced and providing a measure of the fidelity with a high signal-to-noise ratio.

The energy eigenstates of the harmonic oscillator $|n\rangle$ form an equally spaced ladder connected by the action of the creation and annihilation operators $\hat{a}^\dagger$ and $\hat{a}$. Alternative state ladders exist, in which each state is a superposition of energy eigenstates. These can be obtained by applying a unitary transformation, with the resulting states $|\hat{U},n\rangle \equiv \hat{U}|n\rangle$ (Fig. 1A). The transformed state ladders have their own annihilation operators $\hat{K}$, which are related to $\hat{a}$ by $\hat{K} = \hat{U}\hat{a}\hat{U}^\dagger$ (the same transformation can be performed for the creation operator). State preparation by reservoir engineering involves the choice of a suitable engineered basis for which cooling to the ground state results in the desired quantum state $|\hat{U},0\rangle$. In our experiments, we can cool in this basis by coupling the oscillator to an ancilla spin. We use an engineered spin-motion coupling Hamiltonian

$$\hat{H}_- = \hbar\Omega(\hat{K}\hat{\sigma}_+ + \hat{K}^\dagger\hat{\sigma}_-) \qquad (1)$$

where Ω is the Rabi frequency and $\hat{\sigma}_+ \equiv |\uparrow\rangle\langle\downarrow|$, $\hat{\sigma}_- \equiv |\downarrow\rangle\langle\uparrow|$ are spin flip operators. This Hamiltonian results in transitions between adjacent levels on the transformed state ladder, correlated with spin flips. The Hamiltonian dynamics are reversible, and thus cannot reduce entropy. To produce a zero-entropy pure state from a general starting state, dissipation is required, which we introduce by optical pumping of the spin. This pumps the oscillator down the engineered state ladder into the desired ground state (Fig. 1B).

We generate Gaussian oscillator states, which are related to the energetic ground state by combinations of displacements and squeezing of the wave packet (*15*). The unitary transformation is then $\hat{U} = \hat{S}(\xi)\hat{D}(\alpha)$, where $\hat{S}(\xi)$ is the squeezing operator and $\hat{D}(\alpha)$ is the displacement operator (*16*). The resulting annihilation operator in the engineered basis is $\hat{K} = e^{i\phi}(\cosh(r)\hat{a} + e^{i\phi_s}\sinh(r)\hat{a}^\dagger - \alpha)$, where $r = |\xi|$ and $\phi_s = \arg(\xi)$. The phase factor ϕ plays no role in our experiments and we set it to zero in the rest of this Report. $\hat{K}$ contains terms that are linear in the creation and annihilation operators for the energy eigenstates, meaning that the Hamiltonian $\hat{H}_-$ can be implemented by simultaneously applying a combination of the carrier ($\hat{H}_c = \hbar\Omega_c\hat{\sigma}_+ + \text{h.c.}$, where h.c. is the Hermitian conjugate), red motional sideband ($\hat{H}_{rsb} = \hbar\Omega_{rsb}\hat{\sigma}_+\hat{a} + \text{h.c.}$), and blue motional sideband ($\hat{H}_{bsb} = \hbar\Omega_{bsb}\hat{\sigma}_+\hat{a}^\dagger + \text{h.c.}$) transitions. Here Ω_c, Ω_{rsb}, and Ω_{bsb} are taken to be complex parameters, containing both the coupling strength and the phase. In our experiments, these Hamiltonians can be realized simultaneously by applying a multifrequency laser field, with each frequency component resonant with one of the transitions (*16*). The squeezing is obtained from the ratio $\Omega_{bsb}/\Omega_{rsb} = e^{i\phi_s}\tanh(r)$, and the displacement from the ratio $\Omega_c/\Omega_{rsb} = -\alpha/\cosh(r)$.

The experiments work with a single $^{40}Ca^+$ ion, which oscillates along a chosen direction with a frequency close to $\omega_z/(2\pi) = 1.9$ MHz. At the start of each experimental run, the ion is initialized by cooling all motional modes close to the Doppler limit using laser light resonant with the dipole transitions at 397 and 866 nm. All coherent manipulations (including the Hamiltonians used for reservoir engineering) make use of the quadrupole transition at 729 nm, isolating a two-state pseudospin system that we identify as $|\downarrow\rangle \equiv |L=0, J=1/2, M_J=+1/2\rangle$ and $|\uparrow\rangle \equiv |L=2, J=5/2, M_J=3/2\rangle$ (*17*). The Lamb-Dicke factor for our laser configuration is $\eta = 0.05$, which means that the experiments are well described by the Lamb-Dicke approximation (*18*). Optical pumping to $|\downarrow\rangle$ is implemented with a combination of linearly polarized light fields at 854, 397, and 866 nm (*16*). The internal electronic state of the ion is read out with state-dependent fluorescence (*16*).

The reservoir engineering is applied directly after the end of the Doppler cooling. We subsequently probe whether the state of the system has reached the dark state for the Hamiltonian $\hat{H}_-$ by optical pumping into $|\downarrow\rangle$, followed by a probe pulse using $\hat{H}_-$. Examples of data for a coherent ($\Omega_{bsb} = 0$) and a squeezed state ($\Omega_c = 0$) are shown in Fig. 2. In both cases, the state approaches a steady state that approximates a dark state of the pumping Hamiltonian. Experimentally, we have implemented two different methods of dissipative pumping. In the first (used for the coherent state data), we repeat a "cycle" involving applying $\hat{H}_-$ for a fixed duration followed by repumping of the internal state. The second method (used for the squeezed state data) involves continuous application of both $\hat{H}_-$ and the spin dissipation. We observe that the motional state pumping is faster in the continuous case. The pulsed method is easier to maintain, as it avoids AC-Stark shifts arising from the repumping laser. It also allows the use of shaped pulses to produce sideband transitions while avoiding undesired off-resonant excitation of the carrier transition (*19*).

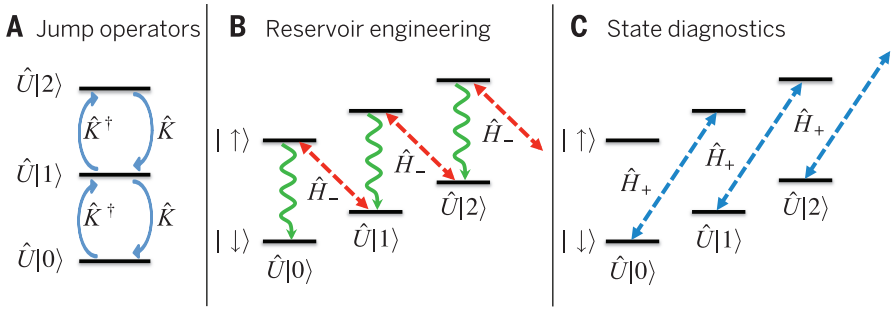

Fig. 1. Cooling and detection using an engineered state ladder. (**A**) The operators $\hat{K}$, $\hat{K}^\dagger$ are ladder operators for the set of basis states $\hat{U}|n\rangle$. (**B**) A combination of the reversible Hamiltonian $\hat{H}_-$ and internal state dissipation leads to pumping into the ground state of the engineered basis. (**C**) State measurement probes the $\hat{H}_+$ Hamiltonian, resulting in single-frequency Rabi oscillations if the system is prepared in $\hat{U}|0\rangle$.

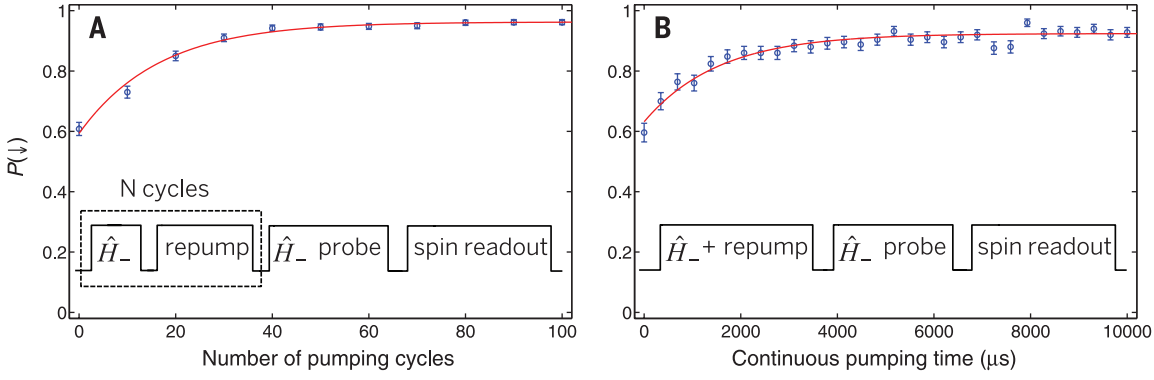

Fig. 2. Onset of the dark state of the reservoir engineering. (**A**) Pulsed preparation of a coherent state. Each pulse cycle consists of applying $\hat{H}_-$ for 25 μs and then repumping the spin. (**B**) Continuous pumping into a squeezed state, in which $\hat{H}_-$ is turned on simultaneously with optical pumping of the spin. The $\hat{H}_-$ analysis pulse lengths are 80 and 55 μs, respectively. In all figures, the data points are the mean measured spin population based on >300 repetitions of the experimental sequence, with error bars estimated from quantum projection noise.

The onset of the dark state indicates that the desired steady state has been reached. We independently verify this state using two methods. The first is a measurement of the populations of the energy eigenstates (*20*), which we perform by pumping the state to $|\downarrow\rangle$ after the end of the reservoir engineering and applying the blue sideband Hamiltonian. The population of the state $|\downarrow\rangle$ as a function of the blue sideband pulse duration t is given by

$$P(\downarrow) = \frac{1}{2}\sum_n p(n)(1 + e^{-\gamma_n t}\cos(\Omega_{n,n+1}t)) \quad (2)$$

where $p(n)$ is the probability of finding the oscillator in the nth energy eigenstate and $\Omega_{n,n+1}$ is the Rabi frequency for the transition between the $|\downarrow\rangle|n\rangle$ and $|\uparrow\rangle|n+1\rangle$ states, which in the Lamb-Dicke regime scales as $\langle n|\hat{a}|n+1\rangle = \sqrt{n+1}$ (*18*, *20*). The phenomenological decay parameter γ_n accounts for decoherence and fluctuations in the applied laser intensities (*16*, *20*). By fitting a form similar to Eq. 2 to each set of data, we obtain the probability distribution $p(n)$ (*16*). We then fit $p(n)$ using the theoretical form of the probability distributions for coherent, squeezed, and displaced-squeezed states (*21*). The data, deduced populations, and fits are shown in Fig. 3. The fit for the coherent state yields a coherent state parameter $|\alpha| = 2.00 \pm 0.01$ (error bars here and elsewhere are given as SEM). For the squeezed state, we obtain a squeezing amplitude $r = 1.45 \pm 0.03$, which for a pure state would correspond to a 12.6 ± 0.3 dB reduction in the squeezed quadrature variance. For the displaced-squeezed state, we obtain fitted parameters of $r = 0.63 \pm 0.06$, $|\alpha| = 2.2 \pm 0.2$, and $\arg(\alpha) - \phi_s/2 = 0.42 \pm 0.06$ rad. The blue sideband method does not allow us to measure the fidelity of the states, because it does not verify the phase coherence of the superposition. It is also difficult to obtain good population estimates for states with a large spread in their Fock state occupancies (*16*). To overcome these limitations, we introduce a diagnosis method that provides a Rabi frequency decomposition in the transformed state ladder that includes the

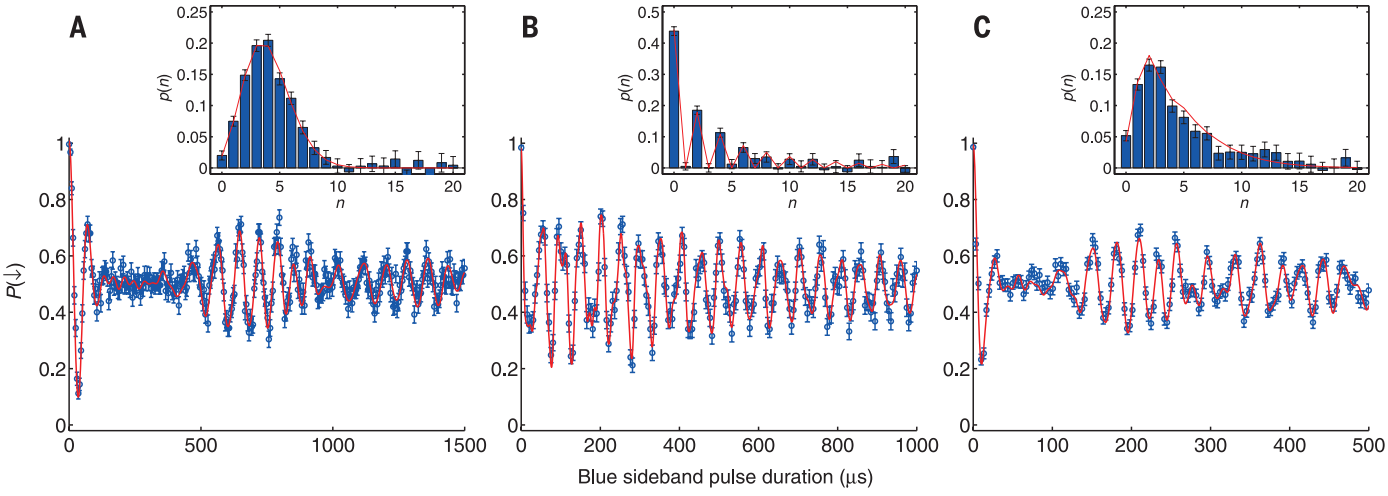

Fig. 3. Fock state analysis using a single-frequency blue-sideband probe. All data are fitted using a form similar to Eq. 2 to retrieve the Fock state populations shown in the inset bar charts. The red curves in the bar charts are fits to the populations using the relevant probability distribution $p(n)$ to determine the size of the states. Data, populations, and fitted distributions are shown for (**A**) the coherent state (with fitted $|\alpha| = 2.00 \pm 0.01$), (**B**) the squeezed vacuum state ($r = 1.45 \pm 0.03$), and (**C**) the displaced-squeezed state ($|\alpha| = 2.2 \pm 0.2$, $r = 0.63 \pm 0.06$ and $\arg(\alpha) - \phi_s/2 = 0.42 \pm 0.06$ rad).

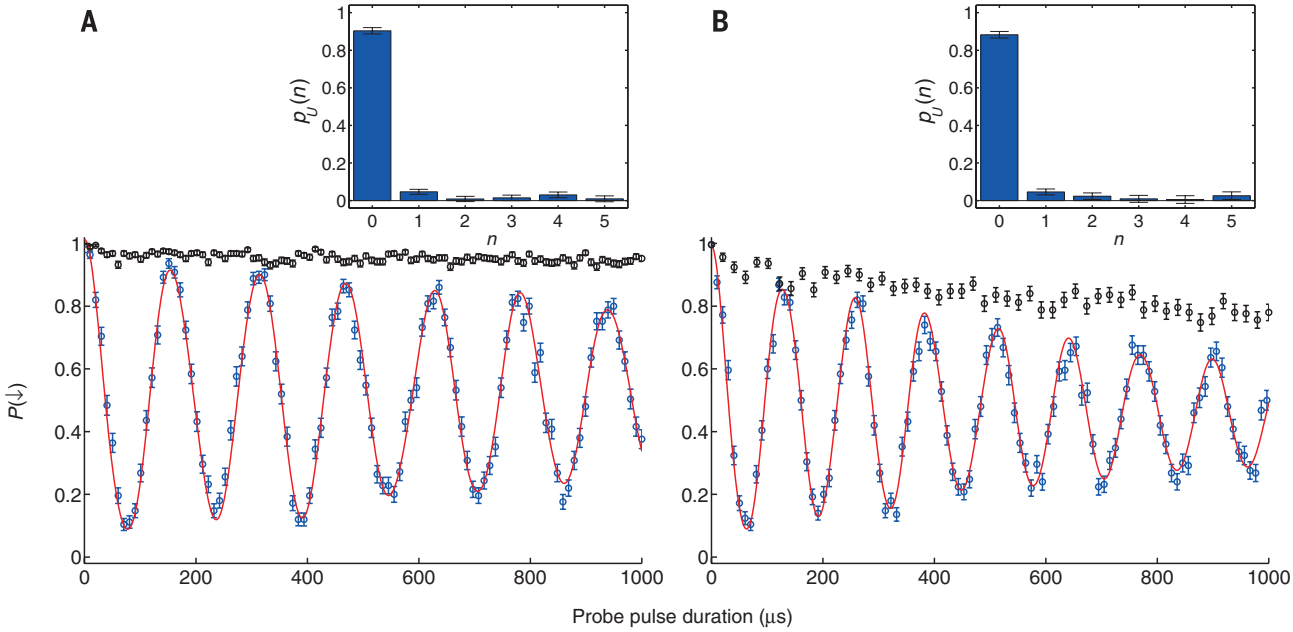

Fig. 4. Fock state analysis in the engineered basis. The data show the spin population evolution after applying $\hat{H}_+$ (blue data points) and $\hat{H}_-$ (black data points) for time t. The fitted curves for $\hat{H}_+$ are of a form similar to Eq. 2. The resulting populations are shown in the inset bar charts. Data and populations are shown for (**A**) the coherent state, with fitted $p_U(0) = 0.90 \pm 0.02$, and (**B**) the squeezed vacuum state, with $p_U(0) = 0.88 \pm 0.02$.

desired state as the ground state. Instead of driving only the blue sideband, we use the Hamiltonian

$$\hat{H}_{+} = \hbar\Omega(\hat{K}^{\dagger}\hat{\sigma}_{+} + \hat{K}\hat{\sigma}_{-}) \quad (3)$$

in which the motional state operators are conjugated with respect to $\hat{H}_{-}$ (Fig. 1C). This results in Rabi oscillations between the states $|\downarrow\rangle|\hat{U}, n\rangle$ and $|\uparrow\rangle|\hat{U}, n+1\rangle$. Because the internal states involved span a two-dimensional Hilbert space, the motional state evolution is also contracted onto two adjacent states of the engineered basis. For an arbitrary initial state, the internal state populations evolve according to Eq. 2, with the corresponding $p(n)$ being the probability of finding the ion in the nth element of the engineered basis before the application of $\hat{H}_{+}$ [we denote this as $p_U(n)$ in the figure to avoid confusion]. Data sets from this type of measurement are shown for the coherent state and for the squeezed state in Fig. 4 for the same settings as used in Figs. 2 and 3. To work in the same basis as the state engineering, we again drive combinations of the carrier and red and blue motional sidebands, but with the ratios of Rabi frequencies calibrated according to $\Omega_c/\Omega_{bsb} = -\alpha^*/\cosh(r)$ and $\Omega_{rsb}/\Omega_{bsb} = e^{-i\phi_s}\tanh(r)$ with ξ and α corresponding to the values used for the reservoir engineering (*16*).

We fit both experimental data sets with a form similar to Eq. 2, obtaining the probability of being found in the ground state of 0.90 ± 0.02 and 0.88 ± 0.02 for the coherent and squeezed states, respectively. We take these to be lower bounds on the fidelity with which these states were prepared, because these numbers include errors in the analysis pulse in addition to state-preparation errors (*16*). The $\hat{H}_{+}$ Rabi oscillations observed in our experiments involve transitions that when viewed in the energy eigenstate basis, couple Hilbert spaces that are of appreciable size. To account for 88% of the populations in oscillations between $|\hat{S}(\xi), 0\rangle$ and $|\hat{S}(\xi), 1\rangle$ for $r = 1.45$, we must include energy eigenstates up to $n = 26$. By our choice of basis, we reduce the relevant dynamics to a two-state system, greatly simplifying the resulting evolution of the spin populations and thus providing a high signal-to-noise ratio. The high fidelity with which the squeezed state is produced is a result of the robust nature of the reservoir engineering, which is insensitive to laser intensity and frequency fluctuations that are common to all frequency components of the engineered Hamiltonian. To generate the same state produced above with standard methods involving unitary evolution starting from the ground state would require simultaneously driving both second motional sidebands (*16*). We would not expect a high fidelity because these have Rabi frequencies comparable to our transition linewidth, which is broadened by magnetic field fluctuations.

This toolbox for generating, protecting, and measuring quantum harmonic oscillator states is transferrable to any physical system in which the relevant couplings can be engineered, facilitating quantum computation with continuous variables (*22*). Examples in which reservoir engineering have been proposed include superconducting circuits and nanomechanics (*12*–*14*). Reservoir engineering provides access to controlled dissipation, which can be used in quantum simulations of open quantum systems (*13*, *23*).

REFERENCES AND NOTES

1. J. I. Cirac, A. S. Parkins, R. Blatt, P. Zoller, *Phys. Rev. Lett.* **70**, 556–559 (1993).
2. J. F. Poyatos, J. I. Cirac, P. Zoller, *Phys. Rev. Lett.* **77**, 4728–4731 (1996).
3. A. R. R. Carvalho, P. Milman, R. L. de Matos Filho, L. Davidovich, *Phys. Rev. Lett.* **86**, 4988–4991 (2001).
4. F. Verstraete, M. M. Wolf, J. I. Cirac, *Nat. Phys.* **5**, 633–636 (2009).
5. S. Diehl *et al.*, *Nat. Phys.* **4**, 878–883 (2008).
6. B. Kraus *et al.*, *Phys. Rev. A* **78**, 042307 (2008).
7. F. Pastawski, L. Clemente, J. I. Cirac, *Phys. Rev. A* **83**, 012304 (2011).
8. H. Krauter *et al.*, *Phys. Rev. Lett.* **107**, 080503 (2011).
9. J. T. Barreiro *et al.*, *Nature* **470**, 486–491 (2011).
10. Y. Lin *et al.*, *Nature* **504**, 415–418 (2013).
11. S. Shankar *et al.*, *Nature* **504**, 419–422 (2013).
12. A. Sarlette, J. M. Raimond, M. Brune, P. Rouchon, *Phys. Rev. Lett.* **107**, 010402 (2011).
13. C. Navarrete-Benlloch, J. J. García-Ripoll, D. Porras, *Phys. Rev. Lett.* **113**, 193601 (2014).
14. A. Kronwald, F. Marquardt, A. A. Clerk, *Phys. Rev. A* **88**, 063833 (2013).
15. W. Schleich, *Quantum Optics in Phase Space* (Wiley-VCH, Berlin, 2001).
16. Materials and methods are available as supplementary materials on *Science* Online.
17. C. Roos, Controlling the quantum state of trapped ions, Ph.D. thesis, Universität Innsbruck, Austria (2000).
18. D. J. Wineland *et al.*, *J. Res. Natl. Inst. Stand. Technol.* **103**, 259 (1998).
19. C. F. Roos, *New J. Phys.* **10**, 013002 (2008).
20. D. M. Meekhof, C. Monroe, B. E. King, W. M. Itano, D. J. Wineland, *Phys. Rev. Lett.* **76**, 1796–1799 (1996).
21. H. P. Yuen, *Phys. Rev. A* **13**, 2226–2243 (1976).
22. D. Gottesman, A. Kitaev, J. Preskill, *Phys. Rev. A* **64**, 012310 (2001).
23. C. J. Myatt *et al.*, *Nature* **403**, 269–273 (2000).

ACKNOWLEDGMENTS

We thank J. Alonso, A. Imamoglu, and D. Wineland for comments on the manuscript and useful discussions. We thank J. Alonso, M. Sepiol, K. Fisher, and C. Flühmann for contributions to the experimental apparatus. We acknowledge support from the Swiss National Science Foundation under grant 200021_134776 and through the National Centre of Competence in Research for Quantum Science and Technology (QSIT).

SUPPLEMENTARY MATERIALS

www.sciencemag.org/content/347/6217/53/suppl/DC1
Supplementary Text
Tables S1 to S3
References (*24*–*28*)

9 September 2014; accepted 24 November 2014
10.1126/science.1261033

ORGANIC CHEMISTRY

Rh-catalyzed C–C bond cleavage by transfer hydroformylation

Stephen K. Murphy,[1,2] Jung-Woo Park,[1] Faben A. Cruz,[1] Vy M. Dong[1]*

The dehydroformylation of aldehydes to generate olefins occurs during the biosynthesis of various sterols, including cholesterol in humans. Here, we implement a synthetic version that features the transfer of a formyl group and hydride from an aldehyde substrate to a strained olefin acceptor. A Rhodium (Xantphos)(benzoate) catalyst activates aldehyde carbon-hydrogen (C–H) bonds with high chemoselectivity to trigger carbon-carbon (C–C) bond cleavage and generate olefins at low loadings (0.3 to 2 mole percent) and temperatures (22° to 80°C). This mild protocol can be applied to various natural products and was used to achieve a three-step synthesis of (+)-yohimbenone. A study of the mechanism reveals that the benzoate counterion acts as a proton shuttle to enable transfer hydroformylation.

The cytochrome P450 enzymes have captured the imagination of chemists who seek to emulate their reactivity. For example, monooxygenases motivated the design of catalysts that epoxidize olefins and oxidize C–H bonds (*1*–*4*). This enzyme superfamily also includes various demethylases that break C–C bonds (*5*). In particular, lanosterol demethylase converts aldehydes to olefins by dehydroformylation during the biosynthesis of sterols in bacteria, algae, fungi, plants, and animals (*6*) (Fig. 1A). Inspired by this step in biosynthesis, we sought a transition-metal catalyst for dehydroformylations in organic synthesis.

[1]Department of Chemistry, University of California Irvine, CA 92697-2025, USA. [2]Department of Chemistry, University of Toronto, Ontario M5S 3H6, Canada.
*Corresponding author. E-mail: dongv@uci.edu

To this end, we aimed to trigger C–C bond cleavage (*7*–*11*) by chemoselective activation of aldehyde C–H bonds using Rh-catalysis (Fig. 1B). Over the past 50 years, activating aldehyde C–H bonds with Rh has been thoroughly investigated (*12*); however, the resulting acyl-Rh^{III}-hydrides have been trapped mainly by hydroacylation (*13*) or decarbonylation (*14*, *15*). This common intermediate is also implicated in hydroformylation, which is practiced on an industrial scale using synthesis gas (*16*). Thus, we needed a strategy for diverting the acyl-Rh^{III}-hydride toward dehydroformylation. To date, olefins generated by dehydroformylation have been observed in low quantities during decarbonylations (*15*, *17*, *18*). One report describes the use of stoichiometric Ru for dehydroformylation of butyraldehyde (*19*), and another uses heterogeneous Rh or Pd catalysts for transforming steroidal aldehydes

Quantum harmonic oscillator state synthesis by reservoir engineering

D. Kienzler *et al.*

Science **347**, 53 (2015);
DOI: 10.1126/science.1261033